nature physics

LETTERS

PUBLISHED ONLINE: 17 JULY 2011 | DOI: 10.1038/NPHYS2044

Visualizing the local optical response to extreme-ultraviolet radiation with a resolution of $\lambda/380$

Kenji Tamasaku[1,2]*, Kei Sawada[1], Eiji Nishibori[3] and Tetsuya Ishikawa[1]

Scientists have continually tried to improve the spatial resolution of imaging ever since the invention of the optical microscope in around 1610 by Galileo[1]. Recently, a spatial resolution near $\lambda/10$ was achieved in a near-field scheme by using surface plasmon polaritons[2,3]. However, further improvement in this direction is hindered by the size of metallic nanostructures[2]. Here we show that atom-scale resolution is achievable in the extreme-ultraviolet region by using X-ray parametric down-conversion, which detaches the achievable resolution from the wavelength of the probe light. We visualize three-dimensionally the local optical response of diamond at wavelengths between 103 and 206 Å with a resolution as fine as 0.54 Å. This corresponds to a resolution from $\lambda/190$ to $\lambda/380$, an order of magnitude better than ever achieved. Although the present study focuses on the relatively high-energy optical regions, our method could be extended into the visible region using advanced X-ray sources[4–7], and would open a new window into the optical properties of solids.

The optical response is recognized as a powerful tool to investigate materials and as a useful property for widespread application in science and industry. In spite of its importance, our knowledge of the optical property is quite limited. At present, we can only measure the macroscopic optical response, and cannot see how electrons in materials respond to the light due to the limited spatial resolution. In other words, the charge response can be investigated only at the Γ point, the origin in the momentum space[8]. Such a situation contrasts with the case of the magnetic response, which is measurable over the whole Brillouin zone[9]. For example, inelastic neutron scattering indicates fluctuating stripes in high-temperature superconductors[10,11]. Microscopic structures, such as stripes and orbital order, are observed commonly in so-called strongly correlated electron systems[10,12]. If the optical probe had the atomic resolution to unveil the charge response with large momentum transfer, it could give direct and clear evidence about the charge dynamics of microscopic structures for deeper understanding of the physical properties[11].

Our basic idea to realize super-resolution is that the linear optical susceptibility, $\chi^{(1)}(\mathbf{r})$, is incorporated in the second-order X-ray nonlinear susceptibility, $\chi^{(2)}(\mathbf{r})$. Here, $\chi^{(1)}(\mathbf{r})$ has a microscopic structure on the atomic scale that determines the local optical response. We consider one of the second-order nonlinear processes[13], X-ray parametric down-conversion (PDC) into the optical region, where an X-ray pump photon (labelled as p) decays spontaneously into an X-ray signal photon (s) and an optical idler photon (i). The origin of nonlinearity is considered to be the Doppler shift[14], where the induced charge at the idler frequency scatters X-rays at a different frequency (Fig. 1a). We expect that this nonlinear process reveals the structure of induced charge, similar to X-ray structural analysis. Our picture is confirmed by calculation on the basis of early works[14,15] as the following relation for isotropic systems:

$$\chi_{\mathbf{Q}}^{(1)}(\omega_i) = \frac{2mc\omega_s}{e\theta_{psi}}\chi_{\mathbf{Q}}^{(2)}(\omega_p = \omega_s + \omega_i) \qquad (1)$$

Here, $\chi_{\mathbf{Q}}^{(1)}(\omega_i)$ and $\chi_{\mathbf{Q}}^{(2)}(\omega_p = \omega_s + \omega_i)$ are the $\mathbf{Q}$th Fourier coefficients of $\chi^{(1)}(\mathbf{r}, \omega_i)$ and $\chi^{(2)}(\mathbf{r}, \omega_p = \omega_s + \omega_i)$, respectively, $\mathbf{Q}$ is the reciprocal lattice vector, θ_{psi} is the polarization factor and the other symbols have their ordinary meanings. We note that our interpretation is more general than the early works, which take into account specific electronic states, such as bond charge[14] or valence charge[16], and ignore the core charge. We treat $\chi_{\mathbf{Q}}^{(2)}(\omega_p = \omega_s + \omega_i)$ instead of $\chi^{(2)}(\mathbf{r}, \omega_p = \omega_s + \omega_i)$ itself, because we observe X-ray PDC as nonlinear diffraction (Fig. 1b) and determine $\chi_{\mathbf{Q}}^{(2)}(\omega_p = \omega_s + \omega_i)$ experimentally[17,18]. The structure of local optical response to the idler light is to be reconstructed by the Fourier synthesis: $\chi^{(1)}(\mathbf{r}, \omega_i) = \sum_{\mathbf{Q}} \chi_{\mathbf{Q}}^{(1)}(\omega_i) \exp(i\mathbf{Q}\cdot\mathbf{r})$. Now the diffraction limit is imposed at the X-ray pump wavelength, despite investigating the optical response at the idler frequency.

Figure 1c shows a typical set of rocking curves of the nonlinear diffraction measured with synthetic type IIa diamond[19]. The photon energies are $\hbar\omega_i = 100$ eV, $\hbar\omega_s = 11.007$ keV and $\hbar\omega_p = 11.107$ keV. The rocking curve was measured with the first five $\mathbf{Q}$ for which the Bragg reflection is observable. Three more sets were measured for $\hbar\omega_i = 60$, 80 and 120 eV at the same $\hbar\omega_p$. The estimation of $\chi_{\mathbf{Q}}^{(1)}(\omega_i)$ is not straightforward due to the characteristic asymmetric peaks of the Fano effect[18,20–22]. We determined the magnitude of $\chi_{\mathbf{Q}}^{(2)}(\omega_p = \omega_s + \omega_i)$ by analysing the Fano spectra[22]. Then, $|\chi_{\mathbf{Q}}^{(2)}(\omega_p = \omega_s + \omega_i)|$ was converted to $|\chi_{\mathbf{Q}}^{(1)}(\omega_i)|$ by equation (1) with the polarization factor, $\theta_{psi} = \sin 2\theta_B$, for the present experimental set-up. Here, θ_B is the Bragg angle for $\mathbf{Q}$ at $\hbar\omega_p$. Note that there is no clear sign of X-ray PDC for $\mathbf{Q} = (2\,2\,2)$ (see Supplementary Information for discussion).

Now let us focus on the linear susceptibility at the idler energy (Fig. 2). To compare it at different photon energies, we normalize $|\chi_{\mathbf{Q}}^{(1)}(\omega_i)|$ to $|\chi_0^{(1)}(\omega_i)|$. Here, the average linear susceptibility, $\chi_0^{(1)}(\omega_i)$, is calculated from the tabulated refractive index[23]. We corrected the local field effect on the macroscopic linear susceptibility using the Lorentz model[8], although the amount of correction is a few per cent. The linear structure factor, namely the Fourier transform of charge density, of the core (valence) electrons, $F_{\mathbf{Q}}^{C}$ ($F_{\mathbf{Q}}^{V}$), is plotted for comparison. We estimated $F_{\mathbf{Q}}^{V}$ using the structure factor measured by X-ray powder

[1]RIKEN SPring-8 Center, 1-1-1 Kouto, Sayo-cho, Sayo-gun, Hyogo 679-5148, Japan, [2]PRESTO, Japan Science and Technology Agency (JST), 4-1-8 Honcho, Kawaguchi, Saitama 332-0012, Japan, [3]Department of Applied Physics, Nagoya University, Furo-cho, Chikusa, Nagoya 464-8603, Japan.
*e-mail: tamasaku@riken.jp.

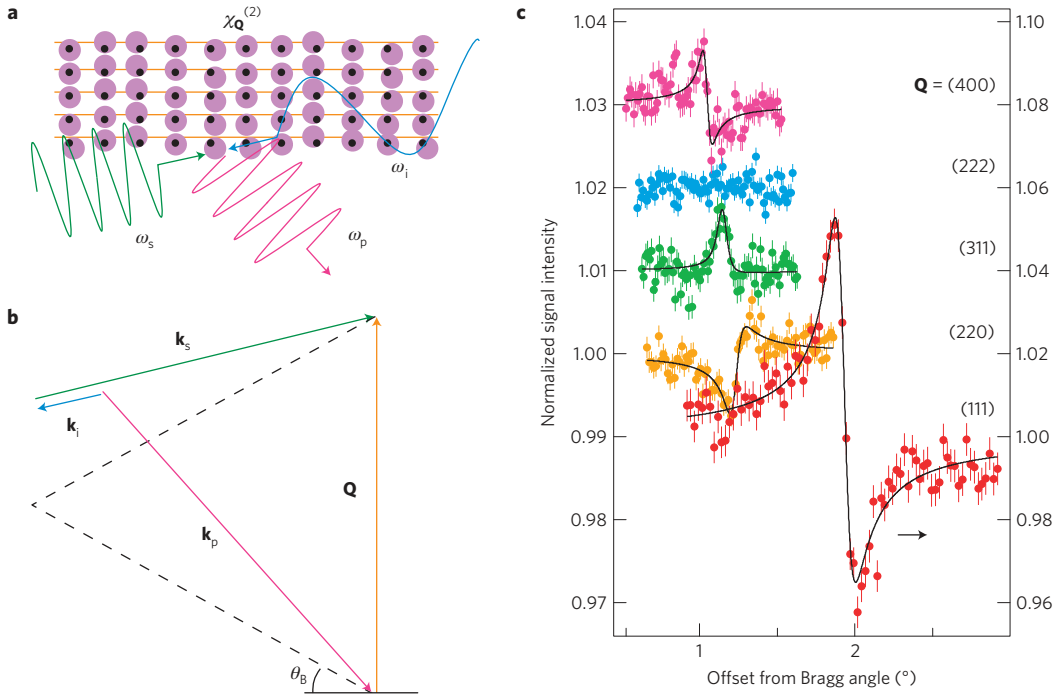

Figure 1 | X-ray PDC and nonlinear diffraction. a, Schematic representation of X-ray PDC into the optical region, which is understood as the following inverse process. The optical (idler) wave oscillates electrons in the nonlinear crystal. The X-ray (signal) wave illuminating the nonlinear crystal is scattered at a different frequency because of the Doppler shift. The reflected X-ray (pump) wave has a sum (difference) frequency of the two waves. **b**, The phase-matching geometry used in this work. The phase-matching condition (momentum conservation) required for X-ray PDC is fulfilled as $\mathbf{k}_p+\mathbf{Q}=\mathbf{k}_s+\mathbf{k}_i$, where $\mathbf{k}$ is the wave vector in the nonlinear crystal. Thus, X-ray PDC is observed as a nonlinear diffraction from a grating of $\chi_{\mathbf{Q}}^{(2)}(\omega_p=\omega_s+\omega_i)$. The exact phase matching is realized at a glancing angle slightly larger than the Bragg angle, θ_B. The dashed lines indicate the usual Bragg diffraction. **c**, The rocking curve measured at an energy of the signal wave, $\hbar\omega_s=11.007$ keV, for five $\mathbf{Q}$: (1 1 1), (2 2 0), (3 1 1), (2 2 2) and (4 0 0). The idler energy is $\hbar\omega_i=100$ eV. Note that the rocking curve corresponds to the phase-mismatch dependence as understood from **b**. Each rocking curve is normalized to the background, which consists of inelastic Compton scattering. The Compton scattering interferes quantum mechanically with X-ray PDC, resulting in the Fano effect. The solid lines indicate fitting with the Fano formula to estimate $\chi_{\mathbf{Q}}^{(2)}(\omega_p=\omega_s+\omega_i)$. The error bars are derived from the square root of row detector counts.

diffraction[24] and calculated $F_{\mathbf{Q}}^{C}$ with the XD2006 program[25]. The $|\mathbf{Q}|$ dependence of $|\chi_{\mathbf{Q}}^{(1)}(\omega_i)/\chi_0^{(1)}(\omega_i)|$ shows rapid decay similar to that of $|F_{\mathbf{Q}}^{V}|$, indicating that $\chi^{(1)}(\mathbf{r},\omega_i)$ is not localized, but extended. At the same time, we notice a longer tail of $|\chi_{\mathbf{Q}}^{(1)}(\omega_i)/\chi_0^{(1)}(\omega_i)|$ at larger $|\mathbf{Q}|$, which is due to a weak contribution from the localized core electrons. These observations indicate that the bond-charge model[14] is not sufficient to describe X-PDC into the extreme-ultraviolet region. The strong $\hbar\omega_i$ dependence of $|\chi_{\mathbf{Q}}^{(1)}(\omega_i)/\chi_0^{(1)}(\omega_i)|$, especially for the smaller $|\mathbf{Q}|$, relates to a change in the structure of $\chi^{(1)}(\mathbf{r},\omega_i)$.

Our key result shown in Fig. 3a–d represents the Fourier-synthesized microscopic structure of linear susceptibility, $\chi^{(1)}(\mathbf{r},\omega_i)$, for the light with the idler energies. The resolution is estimated to be $0.61\times 2\pi/|\mathbf{Q}_{max}|=0.54$ Å (ref. 1), which is much shorter than the idler wavelengths (corresponding photon energies), ranging from 103 Å(120 eV) to 206 Å (60 eV). The resolution in the unit of λ reaches $\lambda/380$ for $\hbar\omega_i=60$ eV, which is the highest ever achieved. As shown in Fig. 3g, we succeed in reconstructing the three-dimensional structure of $\chi^{(1)}(\mathbf{r},\omega_i)$ with a 0.54 Å resolution. It is the most interesting finding that small spherical regions around each atom respond in phase to the light, whereas disc-shaped regions, which respond in the opposite phase, have a stronger contribution and dominate the optical response. The weak structures in the outer region are artefacts of the Fourier synthesis with a limited value of $\chi_{\mathbf{Q}}^{(1)}(\omega_i)$. Note that $\chi^{(1)}(\mathbf{r},\omega_i)$ is normalized to its negative average level, $\chi_0^{(1)}(\omega_i)$.

An important point to be noted in the Fourier synthesis is the phase problem due to the fact that we measured only the amplitude

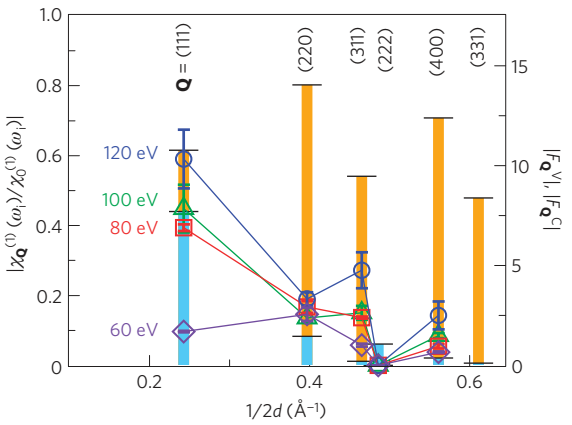

Figure 2 | Fourier coefficients of linear susceptibility, and the structure factors. The $|\mathbf{Q}|$ dependence of the normalized linear susceptibility, $|\chi_{\mathbf{Q}}^{(1)}(\omega_i)/\chi_0^{(1)}(\omega_i)|$, is plotted for $\hbar\omega_i=60$, 80, 100 and 120 eV. The structure factors for the core ($F_{\mathbf{Q}}^{C}$, blue bars) and the valence ($F_{\mathbf{Q}}^{V}$, orange bars) electrons are shown for comparison. The net-plane spacing, $d=2\pi/|\mathbf{Q}|$, is used on the abscissa axis in the conventional manner. The error bars represent statistical and fitting uncertainties.

of $\chi_{\mathbf{Q}}^{(1)}(\omega_i)$. At present, we do not have any established procedure to recover the missing phase, and carry out an exhaustive search. We synthesize $\chi^{(1)}(\mathbf{r},\omega_i)$ using all possible combinations of the phase, and find a structure compatible with physical pictures, such that

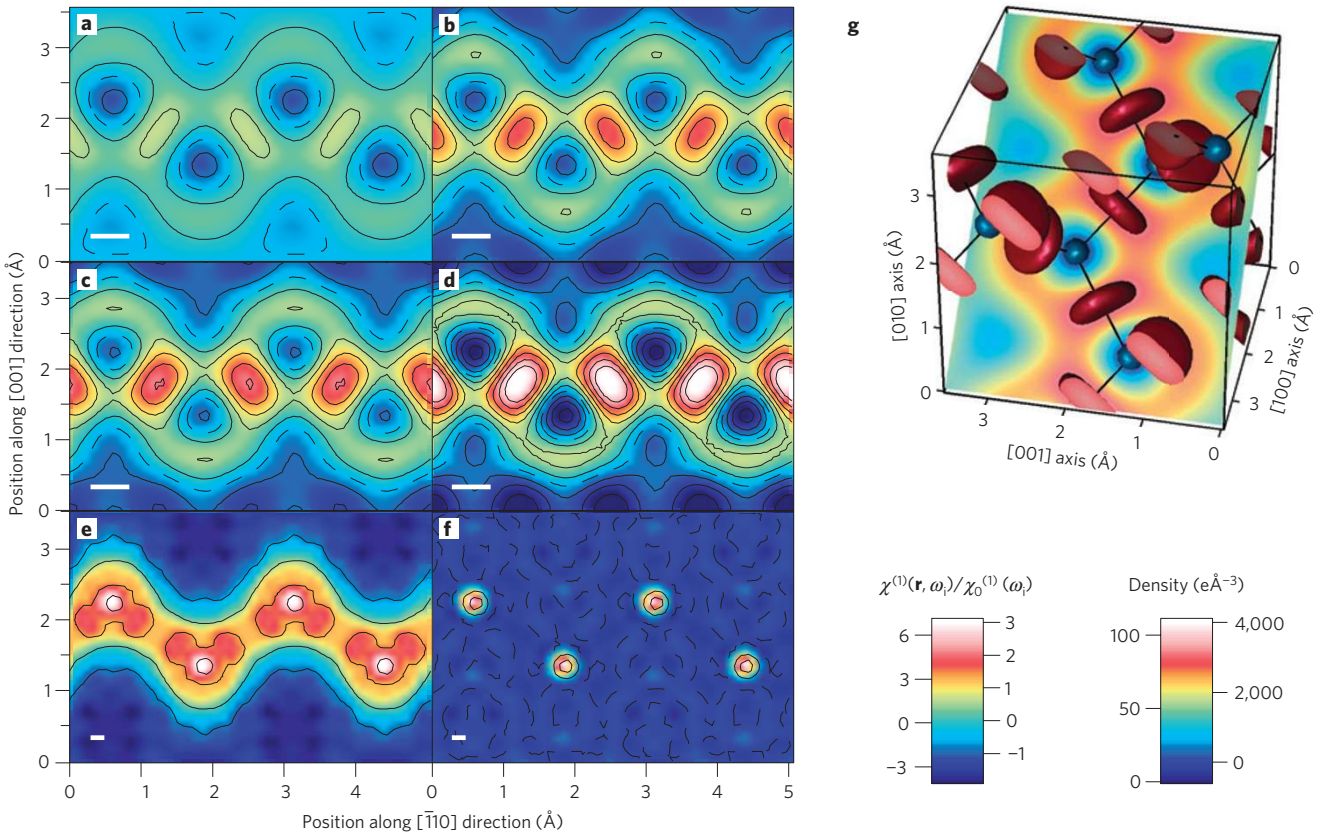

Figure 3 | Reconstructed microstructures of the optical linear susceptibility and the density distribution of valence and core electrons. a–d, The 110-plane cuts of the normalized linear susceptibility, $\chi^{(1)}(\mathbf{r},\omega_i)/\chi_0^{(1)}(\omega_i)$, for $\hbar\omega_i = 60$ eV (**a**), 80 eV (**b**), 100 eV (**c**) and 120 eV (**d**). See the left tick marks of the left colour bar. The contour lines are plotted with an interval of 1.0. The dashed lines indicate the level of $\chi^{(1)}(\mathbf{r},\omega_i)/\chi_0^{(1)}(\omega_i) = 0$. The white bar indicates the resolution of reconstruction, 0.54 Å. **e**,**f**, The 110-plane cuts of the valence (**e**) and the core (**f**) electron density synthesized from $F_{\mathbf{Q}}^{C}$ and $F_{\mathbf{Q}}^{V}$, respectively. We used 43 Fourier components up to $\mathbf{Q} = (8\,8\,0)$. See the left tick marks of the right colour bar for **e** and the right tick marks for **f**. The contour lines are plotted with an interval of 25 e Å^{-3} for **e** and 1,500 e Å^{-3} for **f**. The dashed lines indicate the zero level. The white bar indicates the resolution of reconstruction, 0.19 Å. **g**, Three-dimensional view of $\chi^{(1)}(\mathbf{r},\omega_i)/\chi_0^{(1)}(\omega_i)$ at $\hbar\omega_i = 60$ eV with the 110-plane cut. See the right tick marks of the left colour bar. The red discs and the blue spheres indicate the constant-height surface of $\chi^{(1)}(\mathbf{r},\omega_i)/\chi_0^{(1)}(\omega_i) = 1.9$ (red) and −1.0 (blue), respectively. The blue spheres respond in phase to the light, whereas the red discs in the opposite phase. Note that $\chi_0^{(1)}(\omega_i)$ is negative. Each carbon atom resides at the centre of a blue sphere. The black lines indicate the bonding directions.

$\chi^{(1)}(\mathbf{r},\omega_i)$ should be small in the region where the electron density is low and the bonding sites should have a major contribution (see Supplementary Information for details). The number of combinations can be reduced greatly by the following considerations. As we investigate the optical response far from resonances, we regard $\chi^{(1)}(\mathbf{r},\omega_i)$ as real. Then, $\chi_{\mathbf{Q}}^{(1)}(\omega_i)$ is real, because the diamond structure possesses a centre of inversion. We need to determine only the sign of $\chi_{\mathbf{Q}}^{(1)}(\omega_i)$. The symmetry of the diamond structure fixes the relative phase difference among different $\mathbf{Q}$ with the same magnitude, for example, $\chi_{111}^{(1)}(\omega_i) = -\chi_{11-1}^{(1)}(\omega_i)$.

Before we discuss the microscopic structure of $\chi^{(1)}(\mathbf{r},\omega_i)$, we review the macroscopic optical response of diamonds to make clear what we find. For simplicity, we regard the band structure of diamond as a three-level system, which consists of the 1*s* core level, the valence 'level' and the conduction 'level'. The macroscopic optical response of this three-level system may be described as a sum of two Lorentz oscillators[5]:

$$\chi_0^{(1)}(\omega) = \frac{e^2}{m}\left[\frac{n_c}{\omega_c^2-\omega^2} + \frac{n_v}{\omega_v^2-\omega^2}\right] \qquad (2)$$

Here, n_c (n_v) and ω_c (ω_v) are the number density and the resonance frequency of core (valence) electrons. We ignore the lifetime (damping factor) for simplicity, and assume $\hbar\omega_c = 289$ eV (ref. 22) and $\hbar\omega_v = 12$ eV (ref. 26). It is clear that the valence electron determines $\chi_0^{(1)}(\omega)$ around $\hbar\omega = 100$ eV, because the denominator of the first term is much larger.

According to the macroscopic picture above, it may be thought that the microscopic structure of $\chi^{(1)}(\mathbf{r},\omega_i)$ should be similar to the density distribution of valence electrons. We notice, however, a large difference between them. The valence-electron density (Fig. 3e) has considerable weight at the atomic site, which originates from the 2*s* orbital, whereas $\chi^{(1)}(\mathbf{r},\omega_i)$ at the atomic site is smaller or has opposite sign to the rest (Fig. 3a–d).

The discrepancy between $\chi^{(1)}(\mathbf{r},\omega_i)$ and the density distribution of valence electron is explained well by taking the contribution from the 1*s* core electrons into account. The radii of the *s* orbitals have a quadric dependence on the main quantum number, so the radius of the 1*s* orbital is four times smaller than that of the 2*s* orbital, which makes the density of the 1*s* core electrons 4^3 times higher (Fig. 3e,f). Such a high concentration compensates the larger denominator for the 1*s* core electrons in equation (2). As is clear from equation (2), the 1*s* core electron responds in phase to the light around 100 eV, whereas the 2*s*-like state respond in the opposite phase. The 1*s* core and the 2*s*-like states, which give comparable but opposite contributions to each other, nearly cancel out at the atomic site.

We make a rough estimate of $\chi_{\mathbf{Q}}^{(1)}(\omega_i)$ by replacing n in equation (2) with $F_{\mathbf{Q}}/v_c$, where v_c is the volume of the unit cell.

The 111 structure factors for the 1*s* core electrons and the valence electrons are estimated to be $F_{111}^{C} = -10.8$ and $F_{111}^{V} = -7.70$, respectively[24]. We evaluate equation (2) at $\hbar\omega = 100$eV, and find $\chi_{111}^{(1)}(100\,\mathrm{eV}) = 1.53 \times 10^{-3}$ e.s.u., whereas our experimental result is $(3.7 \pm 0.57) \times 10^{-3}$ e.s.u. The agreement between the calculation and our experimental estimation is considered to be satisfactory for the following reason. As for the average susceptibility, we can compare the calculation by equation (2) with that reported. The calculation gives $\chi_{0}^{(1)}(100\,\mathrm{eV}) = -3.66 \times 10^{-3}$ e.s.u., whereas the reported value is -8.31×10^{-3} e.s.u. (ref. 23). The calculation on the basis of equation (2) gives the same orders of magnitude, and has a tendency to underestimate the susceptibility, which is attributed to the model being simpler than the real band structure.

Finally, we consider qualitatively the energy dependence of $\chi^{(1)}(\mathbf{r}, \omega_i)$. It may be thought naively that only the magnitude of $\chi^{(1)}(\mathbf{r}, \omega_i)$ changes in accordance with $\chi_{0}^{(1)}(\omega_i)$ and that the shape remains unchanged even when the energy of light changes. We find that the shape of $\chi^{(1)}(\mathbf{r}, \omega_i)$ remains basically the same; however, the contrast shows a strong energy dependence. The higher contrast at 120 eV (Fig. 3d) is considered to be due to the stronger resonance effect of 1*s* core electrons at higher photon energies.

In summary, we have demonstrated that we can make use of the spatial resolution of X-rays, keeping the probing wavelength in the optical region, and can visualize the local optical response to extreme-ultraviolet radiation with atomic resolution. The application of our method in a lower-energy region, such as the visible region, requires a deeper understanding of X-ray PDC and a more sophisticated procedure for the phase determination, because the optical response becomes more complicated than equation (2). We discuss briefly a straightforward application of X-ray PDC to the soft-X-ray region. Recently, soft-X-ray resonant scattering has been recognized as a powerful tool to investigate microscopically the strongly correlated system[27]. For example, doped holes in high-temperature superconductors are investigated directly using soft-X-ray resonant scattering at the K edge of oxygen[28]. However, the drawback of using soft X-rays is the limited spatial resolution, 22.8 Å for the oxygen case. Our method should remove this limitation, enlarging the potential of the soft-X-ray probe.

Received 23 March 2011; accepted 8 June 2011; published online 17 July 2011

References

1. Born, M. & Wolf, E. *Principles of Optics* (Cambridge University Press, 1999).
2. Kawata, S., Inouye, Y. & Verma, P. Plasmonics for near-field nano-imaging and superlensing. *Nature Photon.* **3,** 388–394 (2009).
3. Fang, N., Lee, H., Sun, C. & Zhang, X. Sub-diffraction-limited optical imaging with a silver superlens. *Science* **308,** 534–537 (2005).
4. Emma, P. *et al.* First lasing and operation of an ångstrom-wavelength free-electron laser. *Nature Photon.* **4,** 641–647 (2010).
5. Tanaka, T. & Shintake, T. (eds) *SCSS X-FEL Conceptual Design Report* (RIKEN Harima Institute, 2005).
6. Altarelli, M. *et al.* (eds) XFEL: The European X-ray free-electron laser, technical design report. Preprint DESY 2006-097, (DESY, 2006).
7. Kim, K-J., Shvyd'ko, Y. & Reiche, S. A proposal for an X-ray free-electron laser oscillator with an energy-recovery linac. *Phys. Rev. Lett.* **100,** 244802 (2008).
8. Ziman, J. M. *Principles of the Theory of Solids* (Cambridge Univ. Press, 1972).
9. Lovesey, S. W. *Theory of Neutron Scattering from Condensed Matter: Polarization Effects and Magnetic Scattering* (Oxford Univ. Press, 1986).
10. Orenstein, J. & Millis, A. J. Advances in the physics of high-temperature superconductivity. *Science* **288,** 468–474 (2000).
11. Kivelson, S. A. *et al.* How to detect fluctuating stripes in the high-temperature superconductors. *Rev. Mod. Phys.* **75,** 1201–1241 (2003).
12. Tokura, Y. & Nagaosa, N. Orbital physics in transition-metal oxides. *Science* **288,** 462–468 (2000).
13. Adams, B. (ed.) *Nonlinear Optics, Quantum Optics, and UltraFast Phenomena with X-rays* (Kluwer Academic, 2003).
14. Freund, I. & Levine, B. F. Optically modulated X-ray diffraction. *Phys. Rev. Lett.* **25,** 1241–1245 (1970).
15. Eisenberger, P. M. & McCall, S. L. Mixing of X-ray and optical photons. *Phys. Rev. A* **3,** 1145–1151 (1971).
16. Danino, H. & Freund, I. Parametric down conversion of X rays into the extreme ultraviolet. *Phys. Rev. Lett.* **46,** 1127–1130 (1981).
17. Freund, I. & Levine, B. F. Parametric conversion of X-rays. *Phys. Rev. Lett.* **23,** 854–857 (1969).
18. Tamasaku, K. & Ishikawa, T. Interference between Compton scattering and X-ray parametric down-conversion. *Phys. Rev. Lett.* **98,** 244801 (2007).
19. Sumiya, H., Toda, N. & Satoh, S. High-quality large diamond crystals. *New Diamond Front. Carbon Technol.* **10,** 233–251 (2000).
20. Fano, U. Effects of configuration interaction on intensities and phase shifts. *Phys. Rev.* **124,** 1866–1878 (1961).
21. Tamasaku, K. & Ishikawa, T. Idler energy dependence of nonlinear diffraction in $X \rightarrow X + EUV$ parametric down-conversion. *Acta Crystallogr. A* **63,** 437–438 (2007).
22. Tamasaku, K., Sawada, K. & Ishikawa, T. Determining X-ray nonlinear susceptibility of diamond by the optical Fano effect. *Phys. Rev. Lett.* **103,** 254801 (2009).
23. Henke, B. L., Gullikson, E. M. & Davis, J. C. X-ray interactions: photoabsorption, scattering, transmission, and reflection at $E = 50$–$30{,}000$ eV, $Z = 1$–92. *At. Data Nucl. Data Tables* **54,** 181–342 (1993).
24. Nishibori, E. *et al.* Accurate structure factors and experimental charge densities from synchrotron X-ray powder diffraction data at SPring-8. *Acta Crystallogr. A* **63,** 43–52 (2007).
25. Volkov, A. *et al.* XD2006—A Computer Program Package for Multipole Refinement, Topological Analysis of Charge Densities and Evaluation of Intermolecular Energies from Experimental or Theoretical Structure Factors, University at Buffalo, State University of New York, NY, USA; University of Milano, Italy; University of Glasgow, UK; CNRISTM, Milano, Italy; Middle Tennessee State University, TN, USA, 2006.
26. Palik, E.D. (ed.) *Handbook of Optical Constants of Solids* (Academic, 1985).
27. Staub, U. Advanced resonant soft X-ray diffraction to study ordering phenomena in magnetic materials. *J. Phys.: Conf. Ser.* **211,** 012001 (2010).
28. Abbamonte, P. *et al.* Crystallization of charge holes in the spin ladder of $Sr_{14}Cu_{24}O_{41}$. *Nature* **431,** 1078–1081 (2004).

Acknowledgements

We are grateful to T-H. Arima for discussions, and to M. Takata and Y. Tanaka for encouragement. This work was supported by the JST PRESTO program and in part by a grant-in-aid from the Ministry of Education, Culture, Sports, Science and Technology of Japan (2340081).

Author contributions

K.T. and T.I. designed the experiment. K.T. acquired the experimental data, and K.T., K.S. and E.N. carried out the data analysis. K.T. and K.S. wrote the manuscript. All authors discussed the results and commented on the manuscript.

Additional information

The authors declare no competing financial interests. Supplementary information accompanies this paper on www.nature.com/naturephysics. Reprints and permissions information is available online at http://www.nature.com/reprints. Correspondence and requests for materials should be addressed to K.T.